Renovation of Ge-Crystal Monochromator for Neutron Scattering Spectroscopy

A Ge-crystal neutron monochromator was renewed for neutron scattering using hot-pressed Ge pieces of ~40% peak reflectivity. The neutron beam flux from the improved one was increased so that the scattering intensity from a sample was gained by about 60%. We also succeeded in extracting monochromatic neutrons of a second wavelength with a reasonable beam flux.

Neutron scattering spectroscopy is a powerful probe to study phonon and magnon excitations in condensed matter physics. A development of neutron monochromator, which properly branches monochromatic neutrons from a white beam, is therefore one of the instrumental key issues in neutron science; especially, due to the lack of neutron beam flux. Ge and Si single crytals have been one of the typical devices for neutron monochromator, because high-quality and large-size crystals are easily available. However, because of a mismatch between the incident-beam divergence and the small mosaicity coming from perfect crystals, the neutron reflectivity of Ge and Si is severly low and much efforts have been devoted to overcome it.

We have tried to introduce mosaic crystals into Ge crystals appropriately by pressing at high temperatures (Fig.1, left). Eventually, an optimal hot-pressing condition was determined [1,2], so that Ge crystals with a mosaic width of ~0.3° and a peak reflectivity of ~40% are well reproduced (Fig.1, right). A focusing-type Ge monochromator, which was renewed for a KINKEN triple-axis spectrometer AKANE, is shown in Fig.1.

We substituted this renewed monochromator for the previous one on AKANE, and first characterized the beam size of 24*w**32*h* mm^2 at the sample position. This area is about 1.5 times as large as the previous one, and the neutron density per area is confirmed to be unchanged. Second, we radiated the monochromatic neutron beam (λ=2.0 Å) onto relatively large samples and measured scattered-neutron intensity. Figure 2(a) shows a comparison of reflected intensity with previous one. The magnetic Bragg reflections are enhanced in intensity by ~60%, as expected from the beam size. Further, a newly supplied second-wavelength

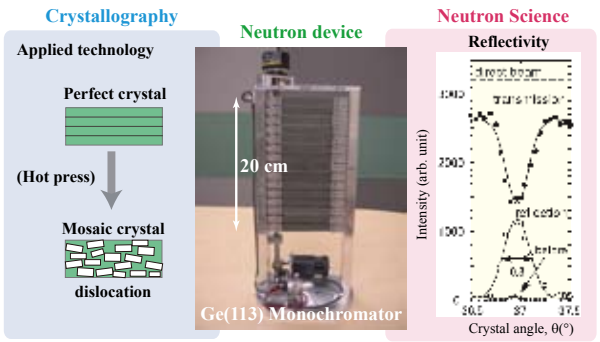

Fig. 1 Neutron crystal monochromator is a product of applied crystallography and promotes neutron science as a fundamental device.

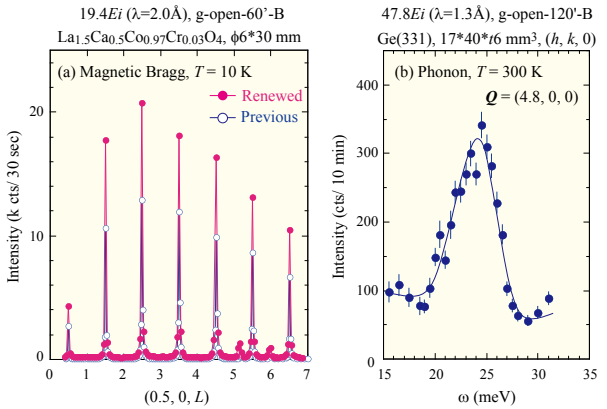

Fig. 2 Spectra measured by the renovated Ge monochromator. (a) Magnetic Bragg reflections for renewed and previous ones. (b) Phonon group measured under the newly equipped second-wavelength mode of λ = 1.3 Å.

mode (λ=1.3 Å) works well for high-energy excitation measurements, as seen in Fig. 2(b). Present renovation not only vitalizes the scientific research on AKANE, but also opens new fundamental techniques on neutron scattering.

References

[1] Y. Miyake, H. Hiraka, K. Ohoyama, Y. Yamaguchi, K. Yamada; J. Phys. (Conf. Ser.) **200**, 112006 (2010).

[2] Y. Miyake, Master Thesis of Science (Tohoku University, Feb. in 2010).

Key Words

Neutron Scattering, Ge Monochromator, Hot Press

Contact to

Haruhiro Hiraka (Metal Physics with Quantum Beam Spectroscopy Division)

E-mail: hiraka@imr.tohoku.ac.jp

URL: http://www.yamada-lab.imr.tohoku.ac.jp/jp/index.html

Strain Accommodation in Martensitic Transformation in Ferrous Alloys

Lath martensite structure becomes more important in recent steel technology due to increasing demands for high-strength structural steels for various applications. Grain refinement in lath martensite is needed for both strengthening and toughening. During growth of martensite, elastic strain is accumulated because of the natures of a displacive transformation. Thus, strain accommodation affects strongly the final crystal sizes of martensite.

Here we report our recent study on mechanisms of strain accommodation during martensitic transformation in Fe-Ni based alloys with advanced crystallographic analyses [1-3].

Optical micrograph of Fig. 1(a) shows a representative morphology of ferrous martensite; 'lenticular martensite'. This morphology is developed in the following sequence; (1) formation of thin-plate martensite seen as 'midrib' which is a straight line inside the martensite; (2) further growth of martensite into a lenticular shape [1]. In the first stage, transformation strain is accommodated mostly by twinning of martensite. In the second stage, possibly due to adiabatic heating, the strain accomodation mode of martensite changes from twinning to dislocation slip. Furthermore, plastic deformation in austenite plays a part of strain accomodation. Thus, high densities of dislocations are introduced inside and outside of the martensite. We have recently developed an advanced method to analyze strain accumulation precisely by image analysis of electron backscatters diffraction (EBSD) patterns [2]. Figure. 1(b) shows the misorientation map of the austenite surrounding the martensite caused by such plastic accommodation. Figure. 1(c) shows variation of the rotation components of the strain tensor measured along the line A-B in (b). There is strain accumulation causing lattice rotation and its distribution is asymmetric. Since it is found that elastic components are negligibly small, it can be concluded that the observed rotations are resulted from the plastic accommodation in austenite. This kind of technique can be applicable to other fields such as an analysis of crack propagation in the brittle fracture.

Plastic accommodation of strain also introduces many dislocations inside the martensite. However, those dislocations are a residue of lattice invariant deformation because dislocation slip needs to penetrate to the austenite/martensite interphase boundary to fully accommodate the strain accumulated. Thus, there must be a high density of dislocations at the boundary.

High-resolution TEM image of Fig. 2(a) shows the atomic structure of an austenite/martensite interphase boundary for the lenticular martensite. There are many lattice dislocations, one of which are enlarged in (b), at the boundary. Quantitative analysis of those dislocations has revealed that there are two sets of dislocations at the boundary in order to accommodate transformation strain effectively.

It has been long considered that growth of martensite occurs by migration of a glisile boundary. A conventional TEM analysis indicated that each set of dislocations is in the form of glissile shear loops. However, once the two sets interact each other or one of those sets interacts with dislocations in the surrounding austenite, sessile dislocation nodes are introduced to the boundary and make

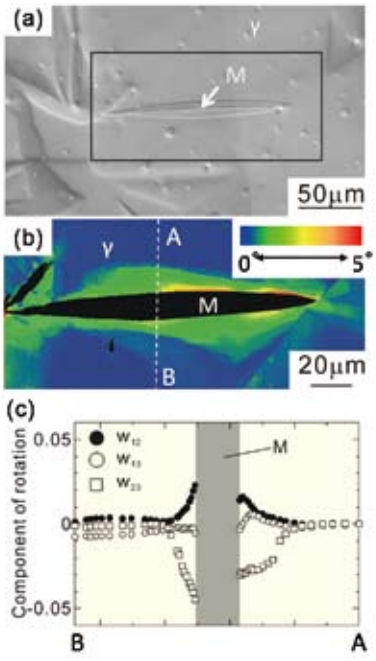

Fig. 1 (a) Optical micrograph of lenticular martensite (M) formed in Fe–33mass%Ni. (b) Misorientation map of austenite (γ) matrix measured by EBSD analysis. (c) Rotation components of the strain tensor in γ along a line A-B.

it more sessile. It is well known that plastic deformation processing of austenite before the martensitic transformation (ausforming) is effective for improvement of strength-toughness balance of martensitic steels. Clearly, the present results provide important information for the effect of plastic accommodation in on the growth of martensite and its final grain size.

References

[1] A. Shibata, S. Morito, T. Furuhara and T. Maki, Acta Materialia, **57**, 483(2009).

[2] G. Miyamoto, A. Shibata, T. Maki and T. Furuhara: Acta Materialia, **57**, 1120(2009).

[3] A. Shibata, T. Furuhara and T. Maki: Acta Materialia, **58**, 3477(2009).

Key Words

High Strength Steel, Phase Transformation, Deformation

Contact to

Tadashi Furuhara (Microstructure Design of Structural Metallic Materials Division)

E-mail: furuhara@imr.tohoku.ac.jp

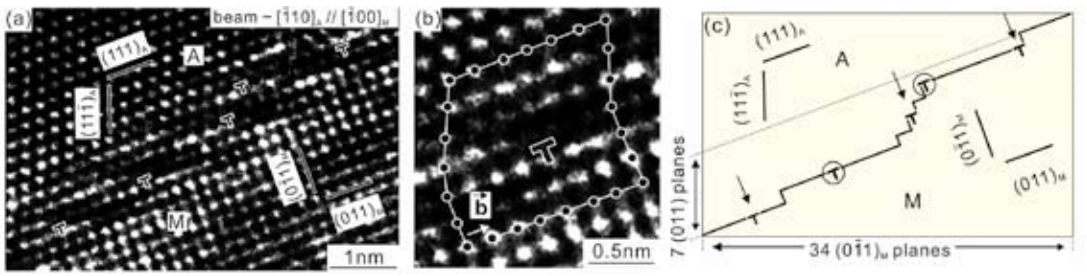

Fig. 2 HREM image showing the interphase boundary of lenticular martensite in Fe–33mass%Ni, viewed along [-1 1 0]A//[-1 0 0]M. (A: austenite, M: martensite), (b) Enlarged atomic structure near the interfacial dislocation in (a). (c) Schematic illustration showing the array of interfacial dislocations in (a).

High Resolution Stress Mapping of the Directionally Solidified Oxide Eutectics by Scanning Near-Field Optical Microscopy

Thermal and transformation-induced strains are suggested to modify the mechanical behavior, which can be studied by means of the piezospectroscopic effect of the luminescence of Cr^{3+} in Al_2O_3. The recently developed scanning near-field optical microscopy (SNOM) technique allows us to obtain the nanometer-scaled residual stress mapping. This new analytical method has been applied for directionally solidified Al_2O_3/ZrO_2 and Al_2O_3/cubic-ZrO_2 (Y_2O_3) eutectics, whch are ranked as candidates for high-strength materials at high temperature.

Directionally solidified eutectic (DSE) samples of Al_2O_3/ZrO_2 and Al_2O_3/cubic-ZrO_2(Y_2O_3) were prepared by the micro pulling down (μ-PD) method using a radio frequency heating system with a pulling rate 1.0 mm/min. Laser-induced fluorescence spectra from the sample surface were collected using the SNOM system which was built into a commercially available AFM (SPM9500J2; Shimadzu Corp.). Excitation laser was a 488 nm line of Ar^+ laser and was focused using a SNOM fiber probe, whose aperture size was 300 nm. It may be added that trace amount of Cr_2O_3 was added to the parent samples in order to improve fluorescence efficiency of Al_2O_3, The further analysis for the position and FWHM of fluorescence line allowed us to discuss the residual stress distribution and its anisotropy.

Very intense red fluorescence is shown by Cr-doped Al_2O_3 (ruby) and its spectrum is widely used as a pressure scale. The fluorescence spectrum of ruby shows two intense sharp peaks in the region of 690–700 nm . The peak at the longer wavelength is called R1; and the other peak at the shorter wavelength is called R2. Figure 1 shows the two-dimensional contoured maps of intensity, position and FWHM of R1. The peak position was converted to stress values. An intense fluorescence region inside the circle in Fig. 1(a) indicates that an Al_2O_3 grain exists inside this circle. On the other hand, a low-intensity region corresponds to the ZrO_2 grains because the fluorescence intensity of ZrO_2 is much weaker than that of Al_2O_3. Stress mapping shown in Fig. 1(b) suggests that tensile stress is increasing toward the center of this circle, thereby indicating that tensile stress is stronger at the center of the Al_2O_3 grain than at the grain boundary between Al_2O_3 and ZrO_2. Furthermore, Fig. 1(c) indicates that the FWHM is larger at the outer part of this circle than the inside. This result suggests that anisotropic stress exists around the Al_2O_3 grain and that it is relaxed near the center of grain. Figure 2 shows the result of the fluorescence intensity measurements in the Al_2O_3/cubic-ZrO_2 (Y_2O_3) DSE. Although an intense fluorescence region again corresponds to an Al_2O_3 grain, the Al_2O_3 grain serves compressive and anisotropic stress and the observed anisotropy was clearly enhanced at the grain boundary between Al_2O_3 and cubic-ZrO_2(Y_2O_3).

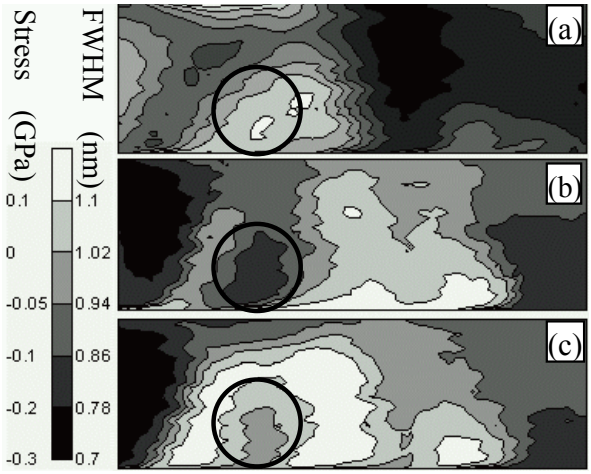

Fig. 1 A fluorescence image of Al_2O_3/ZrO_2 DSE. (a) Peak height of R1 line; (b) peak position of R1 line(stress); (c) FWHM of the R1 line (stress anisotropy).

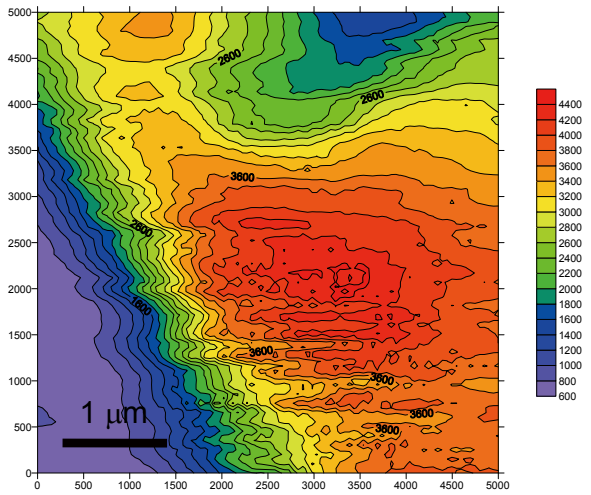

Fig. 2 A fluorescence image of Al_2O_3/cubic-ZrO_2 (Y_2O_3) DSE

References

[1] T. Nakagawa, S.Fukura, M.Nakai, K.Sugiyama,R.Kohara and H.Kagi. Optical Mater., **13**, 269(2006).

[2] S.Fukura, H.Kagi, M.Nakai, K.Sugiyama and T.Fukuda. J.Cryst. Growth, **311**, 998(2009).

Key Words

Al_2O_3/ZrO_2 DSE, SNOM, Stress Mapping

Contact to

Kazumasa Sugiyama (Chemical Physics of Non-Crystalline Materials Division)

E-mail: kazumasa@imr.tohoku.ac.jp

Improvement in Fatigue Strength of Ti-29Nb-13Ta-4.6Zr with Low Young's Modulus

In order to achieve the improvement in fatigue strength of Ti-29Nb-13Ta-4.6Zr (TNTZ) with low Young's modulus, a thermomechanical treatment was optimized in this study[1]. The ω phase, which is likely to increase mechanical strength significantly but decrease ductility drastically in comparison with the α phase, was employed for precipitation strengthening. Further, a short time aging treatment was examined because a small amount of precipitated phase can suppress the increase in Young's modulus. As a result, the fatigue strength of TNTZ could be improved through a short time aging treatment using ω phase precipitation while keeping relatively low Young's modulus.

A biomedical β-type titanium alloy, Ti-29Nb-13Ta-4.6Zr (TNTZ), that is composed of non-toxic and allergy-free elements and exhibits low Young's modulus of around 60GPa after solution treatment, has been developed by our group. In practice, fatigue strength is one of the most important properties for metallic biomaterials. Therefore, in order to improve fatigue strength of TNTZ, various thermomechanical treatments were conducted previously [2]. According to our previous studies, the fatigue strength of TNTZ could be improved up to the same level as a practical titanium alloy, Ti-6Al-4V ELI, by a thermomechanical treatment. However, the Young's modulus of TNTZ was increased above 80GPa by this treatment. In this case, a short time aging is expected to be one of the effective techniques to improve fatigue strength and keep low Young's modulus simultaneously because the amount of precipitate is smaller than the above-mentioned treatment. Further, the ω phase is appropriate as a precipitated phase because this phase increases tensile strength more greatly than the α phase, although too much precipitation of this phase drastically decreases elongation. Therefore, a short time aging at 573K after cold rolling was conducted to introduce a suitable amount of ω phase precipitation, and then the effects of the short time aging on Young's modulus, tensile and fatigue properties of TNTZ were investigated in this study.

The forged TNTZ samples were prepared, and then the samples were subjected to the solution treatment in vacuum at 1063 K for 3.6 ks, followed by water quenching (ST). After the solution treatment, the samples were subjected to the cold rolling in air at room temperature with the reduction ratio of around 90% (CR). Further, the samples were subjected to the aging treatment in vacuum at 573 K for various durations up to 86.4 ks, followed by water quenching (AT).

The Young's modulus decreases slightly after cold rolling and decreases further after the aging treatment up to 0.6 ks. After the Young's modulus decreases once, it increases with aging time. The Young's modulus of the TNTZ samples aged up to 10.8 ks can be kept below the value of 80 GPa.

With regard to tensile properties, the tensile strength increases slightly, but the elongation decreases during cold rolling. Then, the tensile properties do not change much until an aging time of 1.8 ks. However, the tensile strength starts to increase over an aging time of 3.6 ks. The tensile strength and 0.2% proof stress also increase, but the elongation drastically decreases over an aging time of 10.8 ks. At an aging time of 86.4 ks, the tensile strength increases, but the elongation becomes almost zero, and, as a result, the 0.2% proof stress can not be measured.

Figure 1 shows the maximum cyclic stress-fatigue life curves (the number of cycles to failure), i.e., S-N curves, for the TNTZ samples aged for 3.6 ks and 10.8 ks. In this figure, the fatigue limits, which are maximum cyclic stresses at which the samples do not fail at 10^7 cycles, of the solutionized and cold-rolled samples [2] are also shown for comparison. The fatigue limit of the sample aged for 3.6 ks is similar to that of the solutionized and cold-rolled samples. However, in the case of the sample aged for 10.8 ks, the fatigue limit increases remarkably as compared to that of the solutionized and cold-rolled samples.

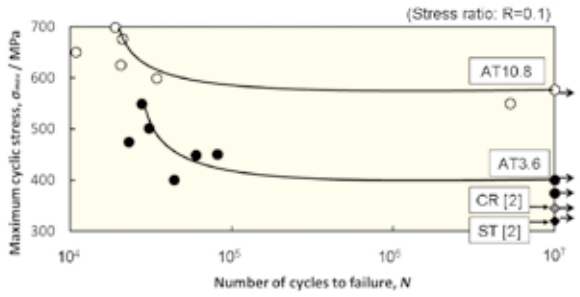

Fig. 1 Fatigue properties of TNTZ aged at 573 K for 3.6 ks (AT3.6) and 10.8 ks (AT10.8) with fatigue limit of cold-rolled and solutionized TNTZ (CR [2] and ST [2], respectively).

References

[1] M. Nakai, T. Akahori, M. Niinomi, H. Tsutsumi and M. Ogawa: Processing and Fabrication of Advanced Materials-XVIII, 2, 787-794 (2009).

[2] T. Akahori, M. Niinomi, H. Fukui, M. Ogawa, and H. Toda, Mater. Sci. Eng. C, 25, 248-254 (2005).

Key Words

Metallic Biomaterial, Thermomechanical Treatment, Mechanical Properties

Contact to

Mitsuo Niinomi (Biomaterials Science Division)

E-mail: niinomi@imr.tohoku.ac.jp

URL: http://biomat.imr.tohoku.ac.jp/

Remarkable Effect of Minor Boron Doping on the Formation of the Largest Size Ni-rich Bulk Metallic Glasses

We reported the formation of a Ni-rich bulk metallic glass with a diameter of 15 mm, the largest size known in Ni-rich alloys. It was found that the minor addition of boron plays a critical role in the dramatic improvement of glass-forming ability of Ni-rich Ni-Pd-P alloy. Thermal and chemical analyses suggest that the improved glass-forming ability is associated with the decrease of fragility rather than impurity scavenging [1].

A series of cylindrical $Ni_{60}Pd_{20}P_{20}$ and $Ni_{60}Pd_{20}P_{17}B_3$ samples with diameters ranging from 6 to 15 mm were prepared by water-quenching (W.Q.) after a B_2O_3 flux treatment. Figure. 1 shows the outer appearances of a ϕ6 W.Q. $Ni_{60}Pd_{20}P_{20}$ sample and a ϕ15 W.Q. $Ni_{60}Pd_{20}P_{17}B_3$ sample. Unlike the ϕ6 $Ni_{60}Pd_{20}P_{20}$ sample, the ϕ15 $Ni_{60}Pd_{20}P_{17}B_3$ sample exhibits a lustrous and smooth surface without any concaves or cavities caused by crystalline phases. XRD and TEM characterization further confirms the amorphous nature of the ϕ15 $Ni_{60}Pd_{20}P_{17}B_3$ sample. The ϕ15 $Ni_{60}Pd_{20}P_{17}B_3$ BMG was the largest Ni-rich BMG reported so far.

For the remarkable effect of boron in the GFA of Ni-rich Ni-Pd-P, at first glance, one may consider that the boron effect comes from oxygen impurity scavenging. To verify this assumption, the oxygen concentration was quantitatively measured. The results show that the difference between the ϕ15 $Ni_{60}Pd_{20}P_{17}B_3$ sample (11 mass ppm) and the ϕ6 $Ni_{60}Pd_{20}P_{20}$ sample (40 mass ppm) is very slight. Thus "self-flux" effect of the added boron in the $Ni_{60}Pd_{20}P_{17}B_3$ alloy is most likely not the main reason that leads to the dramatic improvement in GFA, which is consistent with the previous observation in $Pd_{40}Ni_{40}B_{10}P_{10}$ alloy [2].

The fragility of the $Ni_{60}Pd_{20}P_{20}$ and $Ni_{60}Pd_{20}P_{17}B_3$ alloys were also characterized. From the plots shown in Fig. 2, the fragility parameter (D^*) is determined to be 9 for $Ni_{60}Pd_{20}P_{20}$ and 19 for $Ni_{60}Pd_{20}P_{17}B_3$, respectively. According to the classification of Angell [4], good glass formers are the stronger liquid having larger D*. The larger D^* is corresponding to higher viscosity and lower diffusivity. If steady-state nucleation is assumed, the nucleation rate is determined by effective diffusivity and activation barrier for nucleation at a determined temperature. The decrease of diffusivity will cause a more sluggish kinetics and result in a lower nucleation and growth rate of crystals which are favorable for the stabilization of the supercooled liquid region and the improvement of the GFA. The most likely cause for the liquid behavior change is the much smaller atomic size of boron. The increased mismatch in atomic size makes it possible to produce denser atomic packing, which is related to harder diffusion and higher viscosity in the liquid.

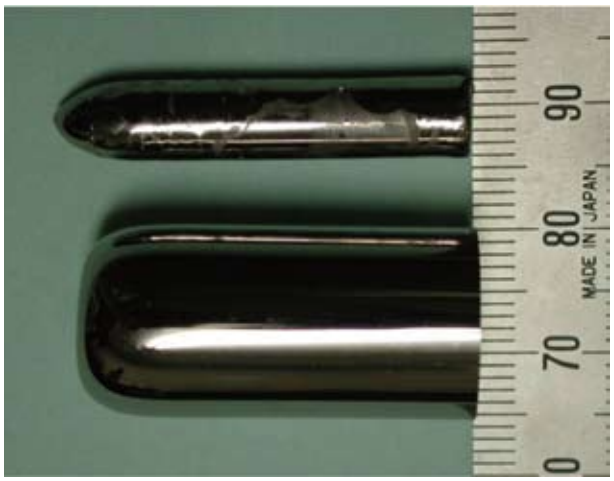

Fig. 1 Outer appearance of the W.Q. $Ni_{60}Pd_{20}P_{20}$ (d = 6 mm) and W.Q. $Ni_{60}Pd_{20}P_{17}B_3$ (d = 15 mm) bulk samples.

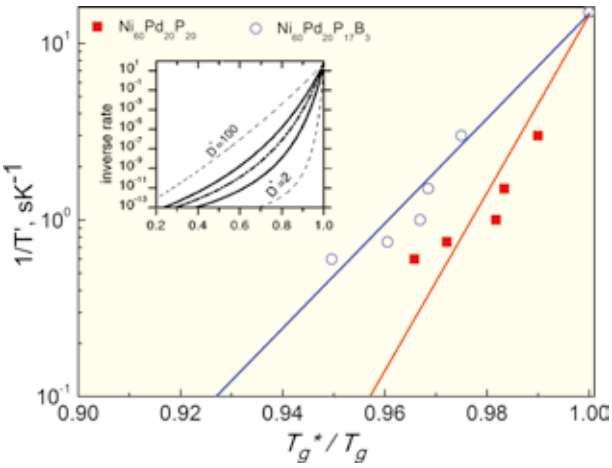

Fig. 2 Fragility plots of the inverse heating rate as a function of T_g normalized to T_g^* measured for glassy $Ni_{60}Pd_{20}P_{20}$ and $Ni_{60}Pd_{20}P_{17}B_3$ at a heating rate of 0.067 K/s. The inset shows the range of D* observed for different materials [3].

References

[1] Y. Zeng, A. Inoue, N. Nishiyama and M. W. Chen, Scripta Mater. 60, 925 (2009).
[2] Q. Li, D. Greig, S.H. Kilcoyne, P.J. Hine, J.A.D. Matthew and G. Beamson, Mater. Sci. Eng. A 408, 154 (2005).
[3] L. Shadowspeaker and R. Busch, Appl. Phys. Lett. 85, 13 (2004).
[4] C. A. Angell, Sci. 267, 1924 (1995).

Key Words

Glass-forming Ability, Impurity Scavenging, Fragility

Contact to

Yuqiao Zeng (Non-Equilibrium Materials Division)
E-mail: zyuqiao@imr.tohoku.ac.jp
URL: http://www.nem.imr.tohoku.ac.jp

Apatite Formation Ability of Ca-P-O System Bioceramic Coatings Prepared by Laser Chemical Vapor Deposition

Ca-P-O system bioceramic coatings, e.g., hydroxyapatite (HAp) and α-, β-tricalcium phosphate, were first prepared by metal organic chemical vapor deposition (MOCVD) and laser chemical vapor deposition (LCVD). (002) oriented HAp films prepared by MOCVD and LCVD exhibited the highest HAp regeneration rate in a pseudo body fluid among all reported values.

Calcium phosphate ceramic materials, such as α-, β-tricalcium phosphate ($Ca_3(PO_4)_2$, TCP) and hydroxyapatite ($Ca_{10}(PO_4)_6(OH)_2$, HAp), are candidate artificial bones and teeth because of their similar structure with human bones and high HAp regeneration rate. However, the mechanical strength and ductility of these materials are too weak for practical usages. Metallic materials, typically Ti-base alloys, are also another candidate possessing high strength and moderate osteoconductivity, whereas the regeneration rate of HAp on Ti–base alloys is insufficient. Therefore, calcium phosphate coated Ti-based alloy can be promising for the biomedical applications.

In the present study, Ca-P-O films were prepared on Ti substrate by MOCVD and LCVD using $Ca(dpm)_2$ and $(C_6H_5O)_3PO$. Hereafter, the results of LCVD are mainly presented. A high power Nd: YAG laser with a beam diameter of 15 mm in a continuous wave mode was irradiated to substrate. The effects of deposition temperature (T_{dep}), laser power (P_L) and Ca to P molar ratio ($R_{Ca/P}$) on crystal phase and microstructure of Ca-P-O films were investigated. The Ca-P-O films were immersed in Hanks' solution at 37 °C for 6 h to 14 d.

β-TCP films in a single phase were obtained on Ti substrate at P_L = 50 W, T_{dep} > 900 K and $R_{Ca/P}$ < 0.4, while HAp films in a single phase were obtained at P_L = 50 W, T_{dep} > 900 K, $R_{Ca/P}$ > 1.0 and T_{dep} < 900 K, $R_{Ca/P}$ > 0.45. The β-TCP films had a (220) orientation with an elongated and angular roof-shaped surface texture, whereas HAp films had a (300) orientation with a granular surface texture [1]. β-TCP and HAp films had a dense cross section. At P_L = 100 W and T_{dep} > 950 K, HAp coating in a single phase with (002) orientation was obtained at $R_{Ca/P}$ = 0.4 to 0.5. At P_L = 200 W and T_{dep} = 1100 to 1400 K, α-TCP coating in a single phase was obtained at $R_{Ca/P}$ < 0.6.

Figure 1 summarizes the apatite formation time on various bioceramic coatings in pseudo body fluid reported in literatures comparing with those of present study. An apatite phase was formed on the MOCVD α-TCP coating after 1 day, and covered the whole specimen surface after 14 d [2]. On the MOCVD HAp coating, an apatite phase was formed after 1 h and covered the whole surface after 6 h [3]. Particle-shaped precipitates were observed on the LCVD α- and β- TCP films after 3 d immersion. However, the precipitate has not wholly covered the films after 14 d immersion. On the LCVD *(300)* oriented HAp coating, needle-shaped precipitates were formed after 12 h and covered the whole surface after 24 h immersion (Fig. 2 left). On the other hand, on the *(002) oriented* HAp coating, precipitates were formed after 3 h and wholly covered

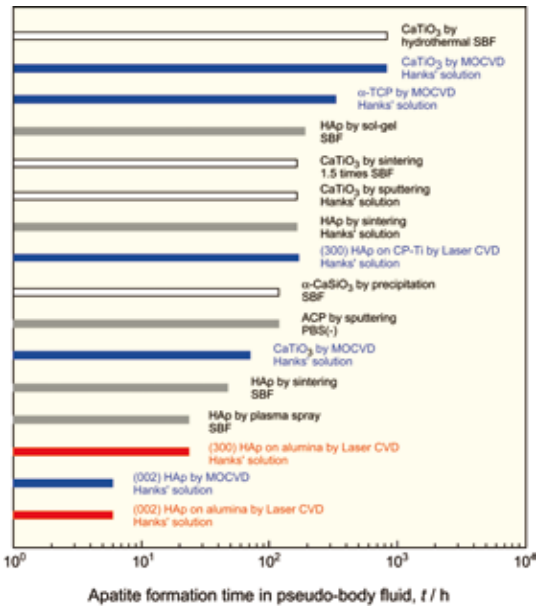

Fig. 1 Apatite formation time on bioceramic coatings prepared by MOCVD and LCVD in a Hanks' solution.

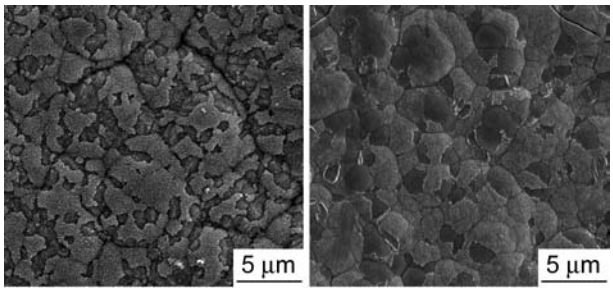

Fig. 2 Surface microstructure of apatite formed on LCVD HAp coatings with (300) (left) and (002) orientation (right) after immersion in Hanks' solution for 24 and 6 h, respectively.

the surface after 6 h (Fig. 2 right). *(002)* oriented HAp prepared by MOCVD and LCVD showed the highest regeneration rate of HAp among literature data reported so far.

References

[1] M. Sato, R. Tu, T. Goto, K. Ueda and T. Narushima: Mater. Trans. **50**, 2455(2009).

[2] M. Sato, R. Tu, T. Goto, K. Ueda and T. Narushima: J. Ceram. Soc. Jpn. **117**, 461(2009).

[3] M. Sato, R. Tu, T. Goto, K. Ueda and T. Narushima: Mater. Sci. Forum **631-632**, 193(2010).

Key Words

Bioceramic Coating, Laser CVD, Hydroxyapatite

Contact to

Takashi Goto (Multi-functional Materials Science Division)

E-mail: goto@imr.tohoku.ac.jp

URL: http://www.goto.imr.tohoku.ac.jp

Novel Grain Refining Technique in Biomedical Co-Cr-Mo Alloy Using Reverse Transformation

Advanced grain refinement of a biomedical Ni-free Co-27Cr-5Mo-0.16N alloy without plastic deformation was successfully achieved by a reverse transformation from lamellar (hcp+M_2N) phases to fcc phase. Our results will contribute to the development of biomedical Ni-free Co-Cr-Mo alloy with refined grain size and good mechanical properties, without requiring any hot workings.

Currently, improved reliability and safety are required for hip and knee joint replacements, since these replacements are being applied in younger patients, greatly prolonging the implants' period of service. Grain refinement is one of the most effective methods of achieving higher mechanical reliability. So far, conventional grain refinement techniques for medical Co-Cr-Mo alloys have involved thermomechanical treatment with recrystallization, such as hot forging, swaging, and rolling, and do result in greatly improved mechanical properties. However, when inhomogeneous strains are introduced during the hot working process, non-uniformly distributed grains are produced. Thus, the mechanical properties inside the part vary from area to area, owing to the non-uniform microstructure. In addition, the conventional techniques are hardly applied to the products fabricated by precise casting, or sintering. Therefore, the advanced grain refinement technique without any plastic deformation process should be considered.

We have advantages for developing advanced grain refining technique in biomedical Co-Cr-Mo alloys since their phase transformation behaviors have been revealed systematicaly in our previous research [1]. Improving the mechanical properties of biomedical Co-Cr-Mo alloy can be achieved using reverse transformation; it is convenient and simple heat treatment.

Figure 1 (a)-(c) show microstructures after solution treatment (the initial state), aging treatment and reverse transformation treatment, respectively [2]. The solution-treated specimen was subjected to aging treatment at 800 °C, forming a lamellar structure of hcp and M_2N phases. Then, the aged specimen having a completely lamellar microstructure was reverse-treated at 1000 °C, where the fcc phase is stable. The resultant grains could be refined from 200 μm to 20 μm, namely approximately 1/10 of their initial size. In addition, the obtained grain obtained by reverse transformation at 1000 °C could be remained constant size (20-25 μm) regardless of holding time. This is the fact that the residual fine M_2N particles could suppress grain coarsening by pinning the grain boundaries. Thus, from the viewpoint of

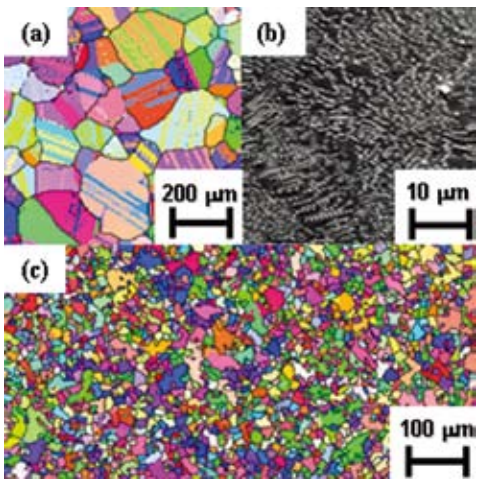

Fig. 1 Microstructure after (a) solution treatment, (b) aging treatment and (c) reverse transformation treatment.

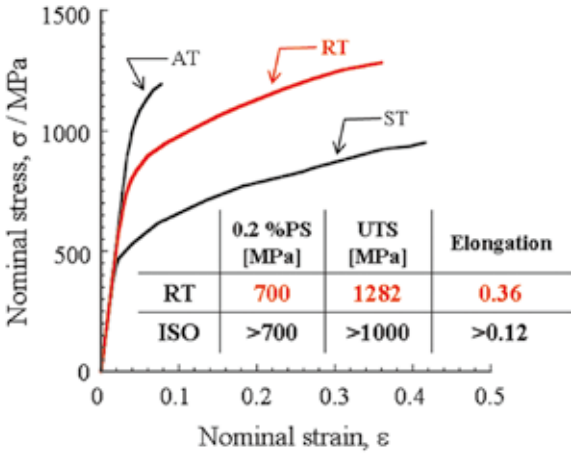

	0.2 %PS [MPa]	UTS [MPa]	Elongation
RT	700	1282	0.36
ISO	>700	>1000	>0.12

Fig. 2 Nominal stress-strain curves of specimens after solution treatment (ST), aging treatment (AT) and reverse transformation treatment (RT). The tensile properties of reverse-transformed specimen and ISO standard (ISO 5832-12) are shown in the table within the figure.

practical application, this slower grain growth is an attractive feature for obtaining homogeneous microstructures in products with complicated shapes or varying thicknesses. Therefore, this technique is widely applicable to biomedical products such as hip and/or knee joints, which are produced by investment casting into various shapes and sizes.

Surprisingly, it was found that the tensile properties of specimens after reverse transformation were superior to those required by the ISO standard for biomedical hot-worked Co-Cr-Mo alloy (ISO 5832-12). Figure 2 show nominal stress-strain curves of specimens after solution treatment (ST), aging treatment (AT), and reverse transformation treatment (RT) [2]. The tensile properties of the reverse transformation specimen and above-mentioned ISO standard are shown in the table inserted in the figure. The tensile properties after reverse transformation exhibited an excellent balance between strength and elongation (ultimate tensile strength:> 1200MPa, elongation: >30%) compared with the alloy without reverse transformation treatment.

The technique presented here, based on heat treatment utilizing reverse transformation, is an effective method for grain size refining without any deformation. Moreover, the technique can be innovated to conventional thermomechanical process since it consists of only heat treatment and hence we will establish the method for further grain refinement and improvement of mechanical reliability in biomedical Co-Cr-Mo alloys at the next step.

References

[1] S. Kurosu, H. Matsumoto and A. Chiba, Proceeding of TMS2010 Meeting.

[2] S. Kurosu, H. Matsumoto and A. Chiba, Mater. Let. **64**, 49 (2010).

Key Words

Grain Refinement, Metallic Biomaterial, Reverse Transformation

Contact to

Akihiko Chiba (Deformation Processing Division)

E-mail: a.chiba@imr.tohoku.ac.jp

URL: http://www.chibalab.imr.tohoku.ac.jp/english/index.php

Bias-current Modulation Technique of a Radio-Frequency Glow Discharge Plasma for Atomic Emission Analysis Associated with a Fast Fourier Transform Analyzer

A measuring method using a fast Fourier transform (FFT) analyzer is suggested to estimate the emission intensity from a radio-frequency (RF)-powered glow discharge plasma for atomic emission analysis. The FFT analyzer has an ability to disperse the components by frequency from an overall signal, and thus works as a selective detector in modulation spectroscopy. In the RF glow discharge plasma, a dc bias current can be introduced by connecting an external electric circuit with the discharge lamp, which predominantly enhances the emission intensities. Further, the bias current can be pulsated with a switching device to modulate the emission intensities, and then the modulated component was selectively detected with the FFT analyzer. This method greatly improved the data precision. The emission intensity of the Cu I 324.75-nm line in an Fe-based alloy sample containing 0.043 mass % Cu could be estimated with a relative standard deviation of 0.20 %. The 3-sigma detection limit of Cu in Fe-based alloys could be obtained to be 2.3 x 10^{-6} mass % Cu for Cu I 324.75 nm.

We have reported that the intensities of particular emission lines are largely elevated when a dc current, which is driven by the self-bias voltage, is introduced into the plasma in RF GD-OES [1]. We call this current a dc bias current. The introduction of the dc bias current could enhance their emission intensities by a factor of 10-20 when atomic emission lines having low excitation energies (3-4 eV) were employed as the analytical line [2]. Furthermore, the dc bias current could be easily pulsated so that a cyclic variation in the emission signal could be selectively detected by using modulation spectroscopic methods. Our previous paper described a detection technique using a lock-in amplifier, which enabled only the modulated component to be detected selectively [3]. In this paper, we report on the analytical characteristics of another detection method using an FFT analyzer, indicating that the emission signals can be measured at very low noise levels and that the analytical precision can be improved greatly [4].

Figure 1 shows the block diagram of the measuring system employed. A glow discharge lamp was made in our laboratory according to the original model of Grimm, where the inner diameter of the hollow anode was 8.0 mm. An RF glow discharge plasma was produced by an RF generator through a matching circuit. A dc self-bias voltage induced in the RF plasma was separated with an RF filter and monitored on a digital voltmeter. By connecting a load resistor with the glow discharge lamp, a dc bias current was conducted through the overall circuit including the plasma body [1]. The current was adjusted by using a variable resistor and it was monitored on a digital ammeter. The bias current could be pulsated with a switching circuit using a photoMOS-relay device, which gave a modulated component of the emission signal at the frequency of switching. Parameters for the switching: the waveform, the frequency and the duty ratio, were pre-determined with a digital function generator. Because the timing pulse is transmitted with the photo-coupling device, leak of the RF power can be completely isolated and thus the switching can be performed with very small distortion. The emission signal was dispersed and detected on a scanning spectrometer, comprising a modified Czerny-Turner mounting monochromator and a photomultiplier tube. An FFT

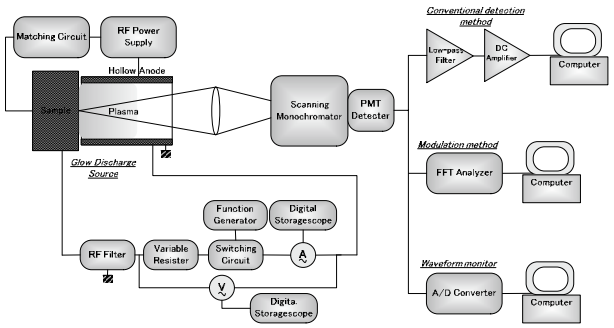

Fig. 1 Block diagram of the measuring system.

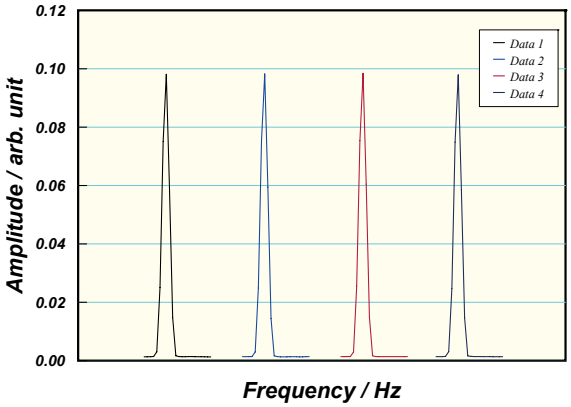

Fig. 2 Reproducibility of the FFT power spectrum in the Cu I 327.45-nm line. Sample: a low-alloyed steel containing 0.043 mass % Cu; rf forward power: 120 W; modulation frequency: 77 Hz (duty ratio of 50%); bias current: 22.6 mA (effective value); the number of averaging: 200; data overlapping on calculation: 60%.

analyzer was employed to detect signal components which were modulated at the frequency of the timing pulse and to remove noise components having any other frequencies. Based on an algorism of the fast Fourier transform, the FFT analyzer yields a power spectrum, where the intensity components are separated by frequency from the overall emission signal. Therefore, only the modulated component can be obtained from the power spectrum. Because the FFT calculation is very fast, the calculator can use a part of the previous data for estimating the next spectrum in the data accumulation. Such overlapping of the data enables a power spectrum to be averaged many times for a short measuring time, and thus averaging of the power spectrum can contribute to an accurate estimation of the intensity data in addition to the removal of noise components having any other frequencies.

Figure 2 shows four-fold measurements of a power spectrum for the emission signal of the Cu I 324.74-nm line when a steel standard sample containing 0.043 mass % Cu is employed. In this case, each spectrum was recorded at a fundamental frequency of 77 Hz and accumulated 200 times at a data overlapping of 60%. These FFT profiles are almost the same as each other, giving an average value of 0.098171 with a standard deviation of 0.000195 (RSD 0.20 %). This result implies that the FFT detection technique can lead to a great improvement in the data precision of the emission intensity when the bias current is modulated. Based on the sensitvity and the signal fluctuation in a blank sample, we could estimate 3-sigma detection limits of 2.3 x 10^{-6} mass % Cu for Cu I 324.75 nm and 6.8 x 10^{-6} mass % Cu for Cu I 327.40 nm. Furthermore, the background equivalent concentration was estimated to be 8.4 x 10^{-4} mass % Cu for Cu I 324.75 nm and 2.6 x 10^{-3} mass % Cu for Cu I 327.40 nm [4].

References

[1] K. Wagatsuma: Spectrochim. Acta, **54B**, 527 (1999).
[2] K. Kodama, K. Wagatsuma: Spectrochim. Acta, **59B**, 429 (2004).
[3] K. Wagatsuma: Anal. Sci., **17**, i65 (2001).
[4] K. Wagatsuma, S. Urushibata: Microchem. J., **95**, 107 (2010).

Key Words

Modulation Spectroscopy, Atomic Emission Spectrometry, Glow Discharge Plasma

Contact to

Kazuaki Wagatsuma (Analytical Science Division)
E-mail: wagatuma@imr.tohoku.ac.jp

Development of Mass Production System for Zr-based Bulk Metallic Glasses

In order to realize the constant quality of bulk metallic glasses (BMGs), mass production system of Zr-based BMGs was newly developed. This mass production system is composed of three machines; weighing-, master alloying- and casting-machines. By making full use of developed mass production system, standardization of BMGs will be accelerated.

Figure 1 shows the outer appearance of automatic weighing machine, which was designed by the combination of shearing and weighing processes. The machine weigh 4-metals i.e. Zr, Cu, Ni and Al, and each metal was cut by shearing to be an objective weight. In actual operation, since it is difficult to cut the Zr metal by its own high strength and high ductility, we adjust the weights of other three metals; Cu, Ni and Al to be an objective alloy composition.

Fig. 1 Outer appearance of automatic weighing machine, *right*: computer and controller board, *left*; shearing and weighing machines with turn table for 15 samples, *back*; materials feeder of three metals, Cu, Ni and Al.

The weight deviation of automatically measure system is about 1 % in this process, we are trying much higher accuracy of this value to be less than 0.5 %. By utilizing the automatic weighing machine, we can suppress the human error and wide weighing deviation.

Figure 2(a) shows the outer appearance of automatic master alloy fabrication machine. There was a semi-automatic arc furnace proposed by DIAVAC ltd. [1], the problem to arrest the development of full-automatic system is the flipping of master alloys. The flipping is an important process to homogenize the deviated composition in master alloy using an arc furnace, and we usually repeat the flipping&remelting process at least 4 times for every master alloys. During the collaborative research between the YKK co. ltd. and Tohoku university, we developed the automatic flipping system [2], and we went into production of full-automatic arc-furnace. We will be able to control the homogenization of master alloys by using this machine. Before the development of this machine, the homogenization of master alloy probably depends on the preparer's skill. In order to achieve the standardization of BMGs, we have to keep on the quality of BMGs and we also standardize the fabrication equipments and those conditions.

To achieve the homogenization of master alloy, we reduce the total weight of the master alloy less than 30 g. We

Fig. 2 Outer appearance of automatic master alloy fabrication machine (a)[1], photo of fabricated $Zr_{55}Cu_{30}Ni_5Al_{10}$ master alloys using the automatic master alloy fabrication machine (b).

can prepare 30 master alloys for one batch, even though the large quantity of a master alloy is a common practice for mass production. This point is completely different from the previous mass production process for BMGs. Figure 2(b) shows photo of $Zr_{55}Cu_{30}Ni_5Al_{10}$ master alloys prepared by this machine. The shining surface as like a mirror points out that the surface region had already vitrified during the solidification on water-cooled Cu-hearth after arc melting [3]. The clear vitrification of almost all master alloys implies the high reproducibility of developed automatic alloying process.

Recently, we are developing an automatic casting process as a next step of described above two processes for the achievement of mass production system for standardization of BMGs. It will be published in elsewhere near future.

References

[1] http://www.diavac.co.jp/

[2] Japanese Patent Application Number: 2009-118159

[3] Y. Yokoyama, H. Fredriksson, H. Yasuda, M. Nishijima and A. Inoue, Mater. Trans., **48**, No6, 1363 (2007).

Key Words

Automatic Weighing Machine, Automatic Master Alloy Fabrication Machine, Standardization

Contact to

Yoshihiko Yokoyama (Advanced Research Center of Metallic Glasses)

E-mail: yy@imr.tohoku.ac.jp